
Stable Port-Hamiltonian Neural Networks

Fabian J. Roth^{1,*}, Dominik K. Klein¹, Maximilian Kannapinn¹, Jan Peters², and Oliver Weeger¹

¹*Cyber-Physical Simulation, Technical University of Darmstadt, Germany*
²*Intelligent Autonomous Systems, Technical University of Darmstadt, Germany*
*Corresponding author, email: roth@cps.tu-darmstadt.de

January 30, 2025

Abstract

In recent years, nonlinear dynamic system identification using artificial neural networks has garnered attention due to its manifold potential applications in virtually all branches of science and engineering. However, purely data-driven approaches often struggle with extrapolation and may yield physically implausible forecasts. Furthermore, the learned dynamics can exhibit instabilities, making it difficult to apply such models safely and robustly. This article proposes stable port-Hamiltonian neural networks, a machine learning architecture that incorporates the physical biases of energy conservation or dissipation while guaranteeing global Lyapunov stability of the learned dynamics. Evaluations with illustrative examples and real-world measurement data demonstrate the model’s ability to generalize from sparse data, outperforming purely data-driven approaches and avoiding instability issues. In addition, the model’s potential for data-driven surrogate modeling is highlighted in application to multi-physics simulation data.

Key words: dynamic systems, physics-guided learning, port-Hamiltonian systems, Lyapunov stability, surrogate modeling

1. Introduction

Recent years have seen strongly growing interest in using machine learning (ML) to identify the dynamics of physical systems directly from observations [5, 28, 31, 32, 39, 41, 50]. This approach has diverse applications, ranging from modeling phenomena with partially or entirely unknown underlying physics to creating surrogate and reduced-order models for rapid simulations and digital twins [23, 50, 51]. In the latter application, data-driven methods can address the drawbacks of traditional numerical methods, which often require tremendous computational resources and expertise [1, 50]. However, in turn,

classical ML algorithms typically require large amounts of training data and lack robustness, as they often suffer from poor extrapolation and are prone to making physically implausible forecasts [1, 33, 50, 51]. To overcome these limitations, a general consensus is to avoid discarding centuries worth of established knowledge in physics, which is an implicit consequence of relying solely on data-driven methods. Instead, there is a growing emphasis on incorporating physical priors and inductive biases into ML approaches [33, 51]. The thus-born field of *physics-guided* ML promises improved accuracy, robustness, and interpretability while reducing data requirements [33, 50].

In recent years, several physics-guided architectures have been proposed for learning dynamical systems. These approaches often parameterize an ordinary differential equation (ODE) to identify continuous-time dynamics. To ensure adherence to the laws of thermodynamics, many architectures build upon modeling frameworks such as Hamiltonian mechanics [9, 15, 20], Lagrangian mechanics [10, 34], Poisson systems [19], GENERIC [17, 52], or port-Hamiltonian systems (PHS) [11, 13, 37, 53]. The latter two frameworks allow for the modeling of dissipative dynamics, while the former are generally limited to energy-conserving systems. Additionally, PHS explicitly incorporate external excitations, making them particularly suited for modeling systems with external control.

The mentioned physical modeling frameworks have implications for the stability of the learned dynamics. For example, stable equilibria in the dynamics of Hamiltonian neural networks correspond to minima or maxima in its Hamiltonian energy function and can never be asymptotically stable. However, these effects are often not discussed in the referenced works. Nevertheless, stability is an important and fundamental property of any dynamic system. Guarantees on the stability of the dynamics may improve the model’s robustness and help trust their predictions. Furthermore, in applications where the physical processes are known to be stable, such guarantees can themselves be viewed as physically motivated biases [14].

Given the importance of the stability property, multiple other works have proposed methods to enhance the stability of learned dynamics. Many use neural ODEs [7] as a basis, as they bridge the gap between dynamical systems and deep learning and provide the opportunity to apply established stability theory. Massaroli et al. [36] propose a provably stable neural ODE variant that reformulates the right-hand side of the ODE as the negative gradient of a scalar function. Consequently, all local minima of this function correspond to stable equilibria with their own basin of attraction. Kolter and Manek [27] describe another provably stable architecture based on neural ODEs and Lyapunov’s stability theory. They concurrently learn unconstrained dynamics with a neural ODE and a convex Lyapunov function. A globally stable equilibrium is guaranteed by projecting the neural ODE-dynamics onto the space of stable dynamics as given by the Lyapunov function. Takeishi and Kawahara [46] extend this approach from a stable equilibrium to stable invariant sets. Other studies have combined Lyapunov’s theory with neural networks (NNs) to guarantee the stability of discrete-time dynamics [14, 29] or to estimate the region of attraction for given dynamical systems [3, 42]. While Lyapunov’s theory primarily addresses stability concerning perturbations in the system’s state, for dynamic systems with inputs, the sensitivity of the state trajectory to these inputs can be equally significant. Kojima and Okamoto [26] propose a projection-based method to learn input-output stable dynamics. Besides the stability of the unforced system, this ensures that the system’s output stays bounded for bounded inputs. In a recent work [38], this projection-based method was generalized to dissipative systems.

While the highlighted studies have either provided stability or physical biases for the data-driven identification of dynamic systems, to the best of the authors’ knowledge, the intersection of these two areas remains largely unexplored. This work aims to exploit the connections between stability and physical frameworks and proposes a port-Hamiltonian NN model for learning stable dynamical systems.

2. Background

2.1. Stability of dynamical systems

We consider autonomous dynamical systems as first-order ODEs

$$\dot{\mathbf{x}} = \mathbf{f}(\mathbf{x}) \quad (1)$$

with $\mathbf{x} \in \mathbb{R}^n$ denoting the systems state and function $\mathbf{f} : \mathbb{R}^n \mapsto \mathbb{R}^n$. Suppose \mathbf{f} is sufficiently smooth to ensure a unique solution of Eq. (1) for any initial condition $\mathbf{x}(t_0)$. A solution $\hat{\mathbf{x}}(t)$ is labeled *stable* in the sense of Lyapunov if, for any small perturbation in the initial condition, the perturbed solution $\bar{\mathbf{x}}(t)$ remains close for

all times, that is, if for any $\epsilon > 0$, there exists a $\delta > 0$ such that $\|\hat{\mathbf{x}}(t_0) - \bar{\mathbf{x}}(t_0)\| < \delta$ implies $\|\hat{\mathbf{x}}(t) - \bar{\mathbf{x}}(t)\| < \epsilon$ for all $t > t_0$ [35, 49]. A stronger version of stability, namely *asymptotic stability*, is obtained if additionally the perturbed solution $\bar{\mathbf{x}}(t)$ converges to $\hat{\mathbf{x}}(t)$ for $t \rightarrow \infty$ for initial conditions $\|\hat{\mathbf{x}}(t_0) - \bar{\mathbf{x}}(t_0)\| < \Delta$ with some $\Delta > 0$ [49].

Lyapunov stability is a *local* property, in the sense that for sufficiently large perturbations, the perturbed solution may stray arbitrarily far even from asymptotically stable solutions [45]. Quantifying the permissible extent of perturbations on the initial condition such that the perturbed solution still converges to the unperturbed solution leads to the concept of a *basin of attraction* [30]. Asymptotically stable equilibria, for which the basin of attraction extends to the entire phase space, are called *globally asymptotically stable* [30]. A system with a globally stable equilibrium cannot have any other equilibria, as their existence would imply that there are solutions (namely the other equilibria) that do not converge to the globally stable equilibrium. For linear ODE systems, stability is always global, i.e., all solutions share the same stability property. In particular, an asymptotically stable equilibrium of a linear system is always globally asymptotically stable.

In the following, we consider the case of an equilibrium solution $\mathbf{x}(t) = \mathbf{0}$, i.e., $\mathbf{f}(\mathbf{0}) = \mathbf{0}$. Placing the equilibrium at the origin is done for ease of notation and is without loss of generality, as arbitrary equilibria can be translated to the origin with a time-independent transformation. The stability of the equilibrium can be determined through the use of Lyapunov’s stability theory by finding a suitable scalar function V called a Lyapunov function [24, 49]. Let $V : D \mapsto \mathbb{R}$ be continuously differentiable and positive definite, that is, $V(\mathbf{0}) = 0$ and $V(\mathbf{x}) > 0$ in $D \setminus \{\mathbf{0}\}$, where $D \subseteq \mathbb{R}^n$ is a neighborhood of the origin. If the value of V is nonincreasing along trajectories of the system in D , then the equilibrium is stable in the sense of Lyapunov. Mathematically, this is the case if $\dot{V}(\mathbf{x})$ is negative semi-definite:

$$\dot{V}(\mathbf{x}) = \frac{\partial V}{\partial \mathbf{x}} \dot{\mathbf{x}} = \frac{\partial V}{\partial \mathbf{x}} \mathbf{f}(\mathbf{x}) \leq 0 \quad \forall \mathbf{x} \in D \setminus \{\mathbf{0}\}. \quad (2)$$

In the case of a negative definiteness ($\dot{V}(\mathbf{x}) < 0$ in $D \setminus \{\mathbf{0}\}$), *asymptotic* stability can be concluded. To obtain *global* asymptotic stability, these conditions must be satisfied *globally*, that is, for all $\mathbf{x} \in D = \mathbb{R}^n$, and the Lyapunov function must be radially unbounded, i.e., $V(\mathbf{x}) \rightarrow \infty$ for $\|\mathbf{x}\| \rightarrow \infty$ [24]. The latter condition avoids the existence of solutions that do not converge to the equilibrium by diverging to infinity without violating the decrease condition in Eq. (2).

2.2. Port-Hamiltonian systems

PHS theory provides a framework for modeling physical systems that generalizes the underlying mathematical structure of Hamiltonian dynamics. It incorporates the modeling of energy-dissipating elements, which are typically absent in classical Hamiltonian systems [48]. Additionally, PHS theory has roots in control theory, emphasizing the interactions of dynamic systems with their environment. In this work, we consider PHS of the form

$$\dot{\mathbf{x}} = [\mathbf{J}(\mathbf{x}) - \mathbf{R}(\mathbf{x})] \frac{\partial \mathcal{H}}{\partial \mathbf{x}}(\mathbf{x}) + \mathbf{G}(\mathbf{x})\mathbf{u}(t). \quad (3)$$

Here, $\mathbf{x}(t) \in \mathbb{R}^n$ describes the system's state, $\mathbf{u}(t) \in \mathbb{R}^m$ its input, and $\mathcal{H} : \mathbb{R}^n \rightarrow \mathbb{R}$ denotes the Hamiltonian, which typically represents the total energy of the system [4, 48]. The skew-symmetric *structure matrix* $\mathbf{J} : \mathbb{R}^n \mapsto \mathbb{R}^{n \times n}$ describes the conservative energy flux within the system. The symmetric positive semi-definite matrix $\mathbf{R} : \mathbb{R}^n \mapsto \mathbb{R}^{n \times n}$ is called *dissipation matrix* and describes the energy losses. Finally, the *input matrix* $\mathbf{G} : \mathbb{R}^n \mapsto \mathbb{R}^{n \times m}$ describes how energy enters and exits the system via the inputs. The matrices are required to satisfy

$$\mathbf{J}(\mathbf{x}) = -\mathbf{J}^\top(\mathbf{x}), \quad \mathbf{R}(\mathbf{x}) = \mathbf{R}^\top(\mathbf{x}) \succeq 0. \quad (4)$$

As direct consequence, PHS extend the energy conservation of Hamiltonian systems to the energy dissipation inequality:

$$\dot{\mathcal{H}} = \underbrace{\frac{\partial \mathcal{H}^\top}{\partial \mathbf{x}} \mathbf{J} \frac{\partial \mathcal{H}}{\partial \mathbf{x}}}_{=0} - \underbrace{\frac{\partial \mathcal{H}^\top}{\partial \mathbf{x}} \mathbf{R} \frac{\partial \mathcal{H}}{\partial \mathbf{x}}}_{\geq 0} + \underbrace{\frac{\partial \mathcal{H}^\top}{\partial \mathbf{x}} \mathbf{G} \mathbf{u}(t)}_{s(\mathbf{x}, \mathbf{u})} \leq s(\mathbf{x}, \mathbf{u}). \quad (5)$$

In the language of system theory, the system is dissipative¹ with respect to the supply rate $s(\mathbf{x}, \mathbf{u})$, which is often stated in the integral form

$$\mathcal{H}(\mathbf{x}(t_1)) - \mathcal{H}(\mathbf{x}(t_0)) \leq \int_{t_0}^{t_1} s(\mathbf{x}, \mathbf{u}) dt. \quad (6)$$

Since the supply rate $s(\mathbf{x}, \mathbf{u})$ is linear in the input \mathbf{u} , it vanishes for zero-input $s(\mathbf{x}, \mathbf{0}) = 0$. The inequality thus ensures that the system cannot gain energy in the absence of an external excitation ($\mathbf{u} = \mathbf{0}$). Besides this physical motivation, the dissipativity property of PHS plays a crucial role in stability analysis. For the unforced system with $s = 0$, the Hamiltonian inherently fulfills the decrease condition $\dot{\mathcal{H}} \leq 0$. Thus, by using \mathcal{H} as a Lyapunov function, it can be shown that any strict minimum in the Hamiltonian implies a stable equilibrium of the unforced dynamics [48]. Furthermore, the equilibrium is asymptotically stable if the system continuously dissipates energy ($\mathbf{R} \succ 0$) for states near the minimum.

¹The technical definition of dissipative systems requires $\mathcal{H} \geq 0$, which will be ensured later. If $\mathcal{H} \in \mathbb{R}$, then the system Eq. (3) is called *cyclo-dissipative*.

3. Stable port-Hamiltonian neural networks

Our goal is to learn the dynamics of physical systems in the form of Eq. (3) with desirable stability properties from observations. To this end, we parameterize the components \mathcal{H} , \mathbf{J} , \mathbf{R} and \mathbf{G} of PHS with NNs.

3.1. Why port-Hamiltonian dynamics?

The use of the port-Hamiltonian formulation has multiple favorable consequences. When learning system dynamics from data, the structure of Eq. (3) provides both a physical bias and the opportunity for interpreting the resulting trained model. Eq. (5) highlights the distinctive roles played by the three matrix-valued functions. The structure matrix $\mathbf{J}(\mathbf{x})$ results in conservative dynamics, the dissipation matrix $\mathbf{R}(\mathbf{x})$ contributes only to the dissipative dynamics, and the input matrix $\mathbf{G}(\mathbf{x})$ captures the energy flow over the system boundaries due to the inputs. This knowledge improves the interpretability of the trained model components. Furthermore, it allows new ways of incorporating prior knowledge into the system. For example, if it is known beforehand that a system conserves energy, then \mathbf{R} can be set to zero. This guarantees that the identified dynamics will exactly conserve the Hamiltonian as long as $\mathbf{u} = \mathbf{0}$.

The energy balance Eq. (5) also demonstrates the physical bias inherently present in Eq. (3). Due to the constraints on \mathbf{J} and \mathbf{R} , the unforced system can only dissipate energy or, at most, conserve it but never gain it. While this property of PHS enforces the thermodynamic constraint that energy cannot be created, its connection to the decrease condition from Lyapunov's theory also provides the opportunity to introduce further desirable stability constraints.

3.2. Stability of port-Hamiltonian dynamics

To guarantee the existence of stable equilibria of port-Hamiltonian systems, it is sufficient to enforce the existence of strict local minima in the Hamiltonian. However, these stability implications are only *local*, meaning the size and shape of the corresponding basin of attraction are not constrained by Eq. (3). Small perturbations might be enough to stray far from the stable equilibria. Furthermore, the general PHS can represent dynamics such as unbounded trajectories, which must be considered unstable from a practical standpoint. The following describes the necessary requirements for achieving *global* stability. Essentially, the Hamiltonian \mathcal{H} is required to be a suitable Lyapunov function, which includes positive definiteness and radial unboundedness. These properties are achieved by constraining the Hamiltonian to be convex and ensuring the existence of a strict minimum. This approach is similar to the construction of a Lyapunov

function by Kolter and Manek [27], but differs in the way the minimum is enforced.

Theorem 3.1. *Consider the PHS Eq. (3) in the unforced case ($\mathbf{u}(t) = \mathbf{0}$), with $\mathbf{J} = -\mathbf{J}^\top$ and $\mathbf{R} = \mathbf{R}^\top$, $\mathbf{R} \succ 0$:*

$$\dot{\mathbf{x}} = [\mathbf{J}(\mathbf{x}) - \mathbf{R}(\mathbf{x})] \frac{\partial \mathcal{H}}{\partial \mathbf{x}}(\mathbf{x}). \quad (7)$$

Suppose the Hamiltonian $\mathcal{H}(\mathbf{x})$ is convex, twice continuously differentiable, and fulfills the following properties:

$$\mathcal{H}(\mathbf{0}) = 0, \quad \left. \frac{\partial \mathcal{H}}{\partial \mathbf{x}} \right|_{\mathbf{x}=\mathbf{0}} = \mathbf{0}, \quad \left. \frac{\partial^2 \mathcal{H}}{\partial \mathbf{x} \partial \mathbf{x}} \right|_{\mathbf{x}=\mathbf{0}} \succ 0. \quad (8)$$

Then, the system in Eq. (7) has a stable equilibrium at $\mathbf{x}(t) = \mathbf{0}$, and all solutions are bounded. Furthermore, the equilibrium is globally asymptotically stable if $\mathbf{R}(\mathbf{x}) \succ 0$.

A proof of Theorem 3.1 is provided in App. A. However, its implications also follow a clear physical intuition. If a dynamical system continuously loses energy via internal dissipation ($\mathbf{R} \succ 0$), it will eventually settle into an energy minimum corresponding to an asymptotically stable equilibrium. The convexity requirement, together with Eq. (8), guarantees the existence of a unique strict and global minimum at the origin. Additionally, it ensures that the energy for states at infinity is unbounded, i.e., $\mathcal{H}(\mathbf{x}) \rightarrow \infty$ as $\|\mathbf{x}\| \rightarrow \infty$. Thus, no finite state has more energy than a state at infinity and all trajectories must be bounded. As a result, all solutions eventually converge to the global energy minimum.

For conservative systems with $\mathbf{R} = \mathbf{0}$, energy is not dissipated, and attractive equilibria cannot exist. Therefore, a conservative system cannot possess asymptotically stable equilibria. Nevertheless, the minimum in the energy still represents a stable equilibrium, and all trajectories stay bounded. The mixed case, where $\mathbf{R} \succeq 0$, only allows the same conclusions as the conservative case. However, in order for a solution $\mathbf{x}(t)$ not to converge to the origin, there must be a time $t^* \geq t_0$ such that $\mathbf{R}(\mathbf{x}(t)) \frac{\partial \mathcal{H}}{\partial \mathbf{x}}(\mathbf{x}(t)) = \mathbf{0} \forall t \geq t^*$. Unless the dissipation matrix vanishes in a large region in phase space, it is unlikely that a system with $\mathbf{R} \succeq 0$ is not globally asymptotically stable.

3.3. Neural network model architecture

Having established the theoretical requirements for stability of PHS, we now outline how these conditions can be met with a dedicated NN model. We call the resulting architecture stable port-Hamiltonian neural network (sPHNN). Its computation graph is illustrated in Fig. 1.

Hamiltonian To fulfill the constraints of Theorem 3.1, the Hamiltonian $\mathcal{H}(\mathbf{x})$ is represented by a fully input convex neural network (FICNN) [2]. FICNNs can approximate any convex function [8]. They are defined by the

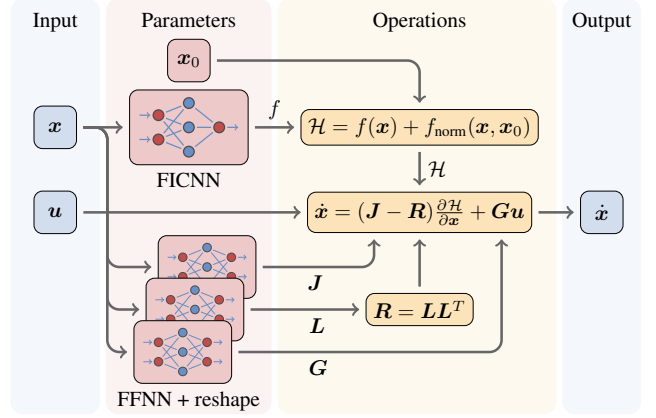


Figure 1. Computation graph of sPHNN. The output of the FFNNs parametrizing \mathbf{J} , \mathbf{L} , and \mathbf{G} are reshaped to be skew-symmetric, lower triangular, and rectangular matrices, respectively.

recurrence relation

$$\begin{aligned} \mathbf{z}_1 &= \sigma_0(\mathbf{W}_0 \mathbf{x} + \mathbf{b}_0), \\ \mathbf{z}_{i+1} &= \sigma_i(\mathbf{U}_i \mathbf{z}_i + \mathbf{W}_i \mathbf{x} + \mathbf{b}_i), \quad i = 1, 2, \dots, k-1, \\ f(\mathbf{x}) &= z_k, \end{aligned} \quad (9)$$

with the pass-through weight matrices \mathbf{W}_i that map the input \mathbf{x} directly to the activation of the $k-1$ hidden layers, bias vectors \mathbf{b}_i , and layer outputs \mathbf{z}_i . If the weight matrices \mathbf{U}_i have non-negative components, the first activation function σ_0 is convex, and all subsequent σ_i are convex and non-decreasing, then the output $f(\mathbf{x})$ is convex in the input \mathbf{x} . Since the Hamiltonian should be twice continuously differentiable, the same must hold for the activation functions. One suitable choice is the soft-plus activation. The conditions for stability in Eq. (8) are fulfilled by representing the Hamiltonian \mathcal{H} with a normalized FICNN:

$$\mathcal{H}(\mathbf{x}) = \underbrace{f(\mathbf{x}) - f(\mathbf{x}_0)}_{f_{\text{norm}}(\mathbf{x}, \mathbf{x}_0)} - \underbrace{\frac{\partial f}{\partial \mathbf{x}} \Big|_{\mathbf{x}_0} \Delta \mathbf{x} + \epsilon \|\Delta \mathbf{x}\|^2}_{f_{\text{reg}}(\mathbf{x}, \mathbf{x}_0)}, \quad (10)$$

with $\Delta \mathbf{x} = \mathbf{x} - \mathbf{x}_0$ and $\epsilon > 0$. The Hamiltonian \mathcal{H} and its gradient vanish at \mathbf{x}_0 due to the normalization term f_{norm} . Moreover, the regularization term f_{reg} containing an arbitrarily small $\epsilon > 0$ ensures positive definiteness of the Hamiltonian's Hessian. However, in practice, f_{reg} can be omitted since the FICNN provides enough bias towards local strict convexity. After training, the stability guarantee can then be recovered by verifying the Hamiltonian's positive definiteness at \mathbf{x}_0 . Choosing $\mathbf{x}_0 = \mathbf{0}$ fulfills all requirements of Theorem 3.1. However, the presented approach is more general. As the assumption that the equilibrium is located at the origin is only made for ease of notation, the normalization approach in Eq. (10) can position the stable equilibrium anywhere in phase space and is not restricted to the origin. If the equilibrium po-

sition is unknown, then it can be inferred from data by optimizing \mathbf{x}_0 during training.

Structure matrix The structure matrix $\mathbf{J} : \mathbb{R}^n \mapsto \mathbb{R}^{n \times n}$ is parameterized by a feed forward neural network (FFNN). As \mathbf{J} is constrained to be skew-symmetric, the matrix has only $k_J = n(n-1)/2$ independent entries. Therefore, the FFNN outputs a vector $\mathbf{c}_J \in \mathbb{R}^{k_J}$ which is then mapped to the space of skew-symmetric matrices via a linear transformation $\mathbf{J} = \mathbf{T}\mathbf{c}_J$, $\mathbf{T} \in \{-1, 0, 1\}^{n \times n \times k}$.

For some applications, \mathbf{J} is independent of \mathbf{x} , and thus, learning a constant \mathbf{J} is sufficient. In particular, this is the case when the conservative dynamics of the system under consideration are Hamiltonian in the given coordinates. Furthermore, by fixing $\mathbf{J} = \mathbf{\Omega}$, where

$$\mathbf{\Omega} = \begin{bmatrix} \mathbf{0} & \mathbf{I} \\ -\mathbf{I} & \mathbf{0} \end{bmatrix} \quad (11)$$

is the symplectic matrix (and choosing $\mathbf{R} = \mathbf{G} = \mathbf{0}$), the sPHNN reduces to a Hamiltonian neural network.

Dissipation matrix Similar to the structure matrix, the dissipation matrix $\mathbf{R} : \mathbb{R}^n \mapsto \mathbb{R}^{n \times n}$ is parameterized by a FFNN. To ensure positive definiteness (or semi-definiteness), the Cholesky factorization $\mathbf{R} = \mathbf{L}\mathbf{L}^\top$ is utilized. Here, \mathbf{L} is a lower triangular matrix with positive (or non-negative) elements along the main diagonal [18]. Similar to the skew-symmetric case of \mathbf{J} , the output $\mathbf{c}_R \in \mathbb{R}^{k_R}$, $k_R = n(n+1)/2$ of the FFNN for \mathbf{R} represents the components of \mathbf{L} . The softplus function is applied to the diagonal elements of \mathbf{L} , ensuring the positive values. For semi-definiteness, the absolute value function is used instead. Analogously to the structure matrix, simple dissipative dynamics might already be sufficiently described with a constant \mathbf{L} .

Input matrix Unlike \mathbf{J} and \mathbf{R} , the input matrix $\mathbf{G} : \mathbb{R}^n \mapsto \mathbb{R}^{n \times m}$ is not subject to any constraints. It is, therefore, directly expressed by a FFNN by reshaping the network’s output vector $\mathbf{c}_G \in \mathbb{R}^{k_G}$, $k_G = nm$ into a matrix. Similar to the other matrices, a constant version of the input matrix that does not depend on the state vector can be used.

3.4. Training stable port-Hamiltonian neural networks

There are two fundamentally different approaches for training sPHNNs: *Derivative* and *trajectory fitting*. The former directly compares the predicted state derivatives $\dot{\mathbf{x}}$ from Eq. (3) to the true derivatives. Although this approach is fast, it requires the true time derivatives to be available as training data, which may not always be the case. Furthermore, derivative fitting is not applicable if augmented states [12] are used, i.e., when the state vector \mathbf{x} is padded with additional dimensions compared

to the observable states in the training data to enrich the representable dynamics. Additionally, a model proficient in predicting the time derivative of the state vector does not necessarily produce accurate predictions for trajectories $\mathbf{x}(t)$, as small derivative errors can accumulate exponentially when integrating an ODE [16]. On the other hand, trajectory fitting directly compares integrated model trajectories $\mathbf{x}(t)$ with ground-truth trajectories, ensuring long-term accuracy. However, the optimization process necessitates either the propagation of the loss gradients through the ODE solver or the use of the adjoint sensitivity method [7], which computes the gradients by solving a modified ODE. In both cases, trajectory fitting incurs significant computational costs due to gradient propagation and model integration, making trajectory fitting much slower than derivative fitting.

A distinct advantage of sPHNNs is the favorable influence the stability constraint exerts on the training process when using trajectory fitting. Neural ODEs and similar architectures can suffer from exploding gradients, where small parameter changes lead to large loss gradients. This can slow the training process or prevent it from converging. A potential cause is the crossing between the boundaries of local basins of attraction during training, leading to significant differences in long-term behavior [40]. Since sPHNNs have only one global basin of attraction, this source of training difficulties is eliminated. In our numerical experiments, we observe good convergence of the training error of sPHNNs where neural ODEs struggle without the use of regularisation terms or gradient clipping.

4. Experiments

We evaluate the proposed model on multiple example problems, including measurement data from a real physical system and multi-physics simulation data. In the experiments, the performance of sPHNNs is compared to that of neural ODEs and port-Hamiltonian neural networks without the stability constraint (PHNNs). All models are trained by minimizing the mean squared error using the ADAM [25] optimizer. Model hyperparameters are listed in App. B. For ODE integration, the Runge–Kutta scheme Tsit5 [47] with an adaptive step size is used.

4.1. Interpreting random sPHNNs

To visualize the physical bias and inherent interpretability of sPHNNs, we show the decomposition into conservative and dissipative dynamics for untrained NNs parameterizing \mathcal{H} , \mathbf{J} , and \mathbf{R} for $n = 2$ in Fig. 2. The trajectories of the conservative dynamics resulting from $\mathbf{J} \partial \mathcal{H} / \partial \mathbf{x}$ exhibit cyclic, energy-conserving behavior and align with the level sets of the Hamiltonian in this two-dimensional case. Conversely, the dissipative dynamics resulting from

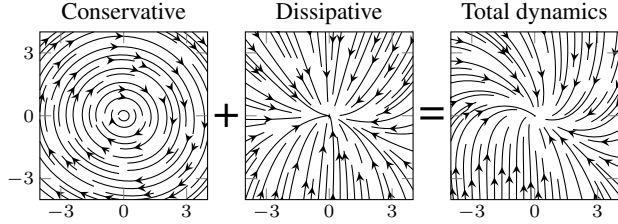


Figure 2. Dynamics of a randomly initialized sPHNN.

$-\mathbf{R}\partial\mathcal{H}/\partial\mathbf{x}$ demonstrate the convergence of solutions to the origin, resulting in the globally asymptotically stable dynamics of the sPHNN.

4.2. Spinning rigid body

We generate data of a damped spinning rigid body by numerically integrating Euler’s rotation equations, see App. C for a detailed description. Here, accurately capturing the dynamics of the angular velocity vector $\mathbf{x} = \boldsymbol{\omega}$ with a PHS requires a state-dependent structure matrix $\mathbf{J}(\mathbf{x})$. We train ten instances per model type using derivative fitting with $(\boldsymbol{\omega}, \dot{\boldsymbol{\omega}})$ pairs sampled from the trajectories. Figure 3 shows the rotational energy $E(\boldsymbol{\omega})$ computed from model predictions $\boldsymbol{\omega}$ via Eq. (C.2) and corresponding outputs of the Hamiltonian NNs $\mathcal{H}(\boldsymbol{\omega})$ for sPHNNs and PHNNs. The former successfully identified the true system’s energy, with the Hamiltonian closely matching the energy computed from its predictions and ground truth, respectively. In contrast, the PHNNs show noticeable deviations between the Hamiltonian and the energy calculated from its predictions, which also do not converge to zero. Furthermore, the neural ODEs show unphysical behavior with increasing energy at certain points and exhibit high variance between instances.

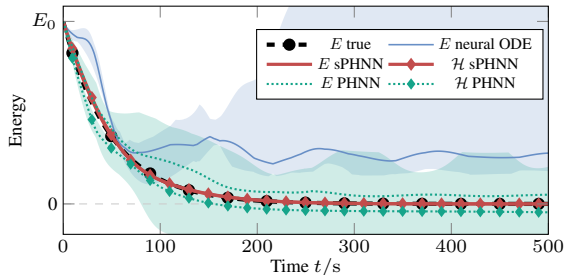
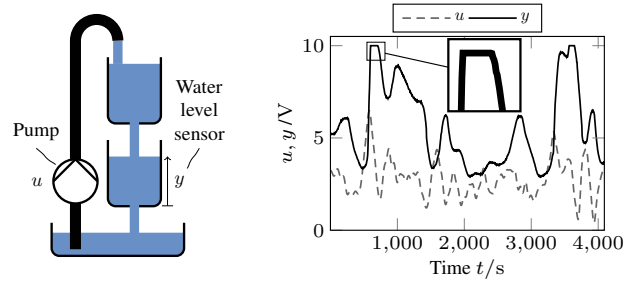


Figure 3. Interquartile mean (lines) and range (shaded regions) of the energy E and Hamiltonian \mathcal{H} of the predicted states.

4.3. Cascaded tanks

Next, the sPHNN model is evaluated using the cascaded tanks data set [43, 44]. It contains measurements of a physical fluid level control system consisting of a pump and two tanks, see Fig. 4a. Liquid flows from the upper tank through an outlet into the lower tank, exits via a similar outlet into a reservoir, and is pumped back up to



(a) Experimental setup (b) Training data (overflow highlighted)

Figure 4. Cascaded tanks experiment setup and training data.

the upper tank. The system’s input u is the voltage applied to the pump, with higher values resulting in a faster volume flow. The fluid level in the lower tank is measured with a capacitive sensor, and the resulting voltage represents the system’s output y . The data consists of two trajectories comprising 1024 pairs (u, y) each. The training trajectory is depicted in Fig. 4b. The initial water level in the upper tank is unknown but is the same for both trajectories.

We model the system using a two-dimensional state vector $\mathbf{x} = [x_1, x_2]^\top$, where $y = x_2$. Assuming the augmented state x_1 describes the water level in the upper tank, it is straightforward to determine the equilibrium of the autonomous system. With zero input, the tanks will eventually drain; therefore, the stable equilibrium is given by $\mathbf{x}_0 = \mathbf{0}$. We thus fix the minimum of the sPHNN’s Hamiltonian to the origin. However, for a general problem, one might have little to no knowledge about the dynamics, and it might be challenging to infer the location of the relevant equilibrium. To investigate the effects of this potential lack of knowledge, we train a second sPHNN version hereafter called sPHNN-LM. Its minimum location \mathbf{x}_0 is initialized randomly and is optimized during training. Apart from this, both sPHNN versions are identical and use a constant fixed symplectic matrix as the structure matrix, as well as constant but learnable dissipation and input matrices. The PHNNs are defined identically to the sPHNNs, except for the use of unconstrained FFNNs instead of the normalized FICNNs.

We train 20 instances per model type and show a statistical evaluation of the root mean squared errors (RMSEs) of the models on both the training and test data in Fig. 5a. Both sPHNN and sPHNN-LM achieve a similar accuracy, whereas the neural ODE and PHNN perform worse on both trajectories on average. Furthermore, the variance between the instances of the sPHNNs is noticeably smaller than for the neural ODE and PHNN.

To evaluate the extrapolation capabilities of the models, we perform two additional experiments. First, we extend the evaluation data with 400 s of zero-input. The resulting predictions are depicted in Figure 5b. Assuming perfectly calibrated sensors, the true system response is an eventual zero-output as both tanks eventually drain.

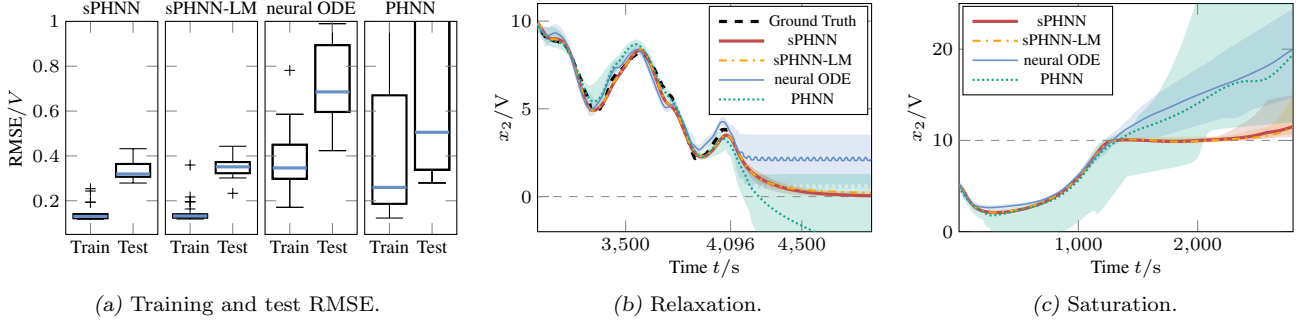


Figure 5. Cascaded tanks evaluation. *Left*: RMSEs for training and test trajectories. *Middle*: Predictions for the extended cascaded tanks test trajectory. At $t = 4096$ s, the pump is turned off. *Right*: Predictions for a linearly increasing pump voltage. Due to an overflow, the true system exhibits a hard saturation at $x_2 = 10$ V. Lines correspond to the interquartile mean, whereas shaded areas represent the interquartile range of the predictions from the 20 model instances.

Per construction, this behavior is guaranteed for sPHNNs. The 20 sPHNN-LM instances identified the equilibrium to be in the range from -0.196 V to 0.432 V, which shows that also \mathbf{x}_0 can be learned reliably. However, the neural ODE and PHNN models exhibit limitations in physically sensible extrapolation. Although some instances predict the water level to converge, the final values span a range of behaviors, including highly unphysical predictions, like oscillating water levels.

In the second extrapolation study, we investigate the hard saturation the cascaded tanks data system exhibits at an output value of 10 V. This occurs when the tanks overflow in response to a large input voltage over an extended period of time (see Fig. 4b) [44]. We explore the models' behavior in this regime by constructing a pump voltage signal that linearly increases from 1 V initially to 8 V at 2800 s. The resulting predictions are shown in Fig. 5c. For pump speeds up to ~ 7 V (~ 2400 s), the sPHNN and sPHNN-LM instances capture the saturation effect, while the neural ODE and PHNN instances fail to do so.

4.4. Thermal food processing surrogate

With the applicability of sPHNNs to real-world data established, this section focuses on one of the promising applications of data-driven dynamic system identification: the efficient construction of surrogate models. Here, data from a conjugate heat transfer simulation in a convection oven coupled with a soft matter model for meats from Kannapinn et al. [21, 23] is employed. The data consists of trajectories representing the temperature histories T_A and T_B at two probe points within the meat. These result from a predefined excitation signal T_{oven} , which controls the oven temperature. The surrogate's task is to predict the probe temperatures given the oven temperature as input.

We fit sPHNNs, neural ODEs, and PHNNs to two trajectories consisting of 280 samples each (see App. D). For each model, we vary the dimensionality of the state variable $\mathbf{x} \in \mathbb{R}^n$ with $n = 2 + n_A$ by adding 0 to 3 augmented

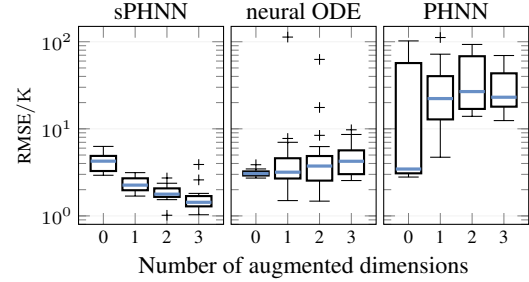


Figure 6. RMSEs of thermal food processing surrogate models evaluated on the 25 test trajectories for varying numbers of augmented dimensions.

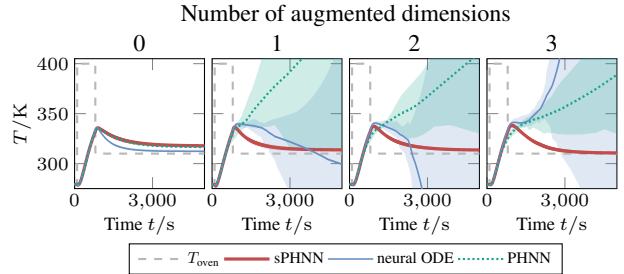


Figure 7. Interquartile mean and range of the T_A predictions for varying number of augmented dimensions for a custom test case.

dimensions n_A . The minimum \mathbf{x}_0 of the sPHNNs' Hamiltonian is set to the point in phase space corresponding to the ambient temperature, as motivated by physical intuition about the stable thermal equilibrium. The initial values of the augmented states are fixed to zero. In total, 20 instances are trained per model type and augmented dimension.

The RMSEs evaluated on 15 test trajectories (see App. D) are depicted in Fig. 6. The sPHNN predictions tend to improve with more augmented dimensions, achieving errors comparable to those obtained by Kannapinn et al. [21] using commercial software. In contrast, the neural ODEs and PHNNs tend to deteriorate in performance with more augmented dimensions, likely due to instabilities in the learned dynamics. This becomes apparent in Fig. 7, which depicts the models' predictions for a custom test case not included in the data set. While

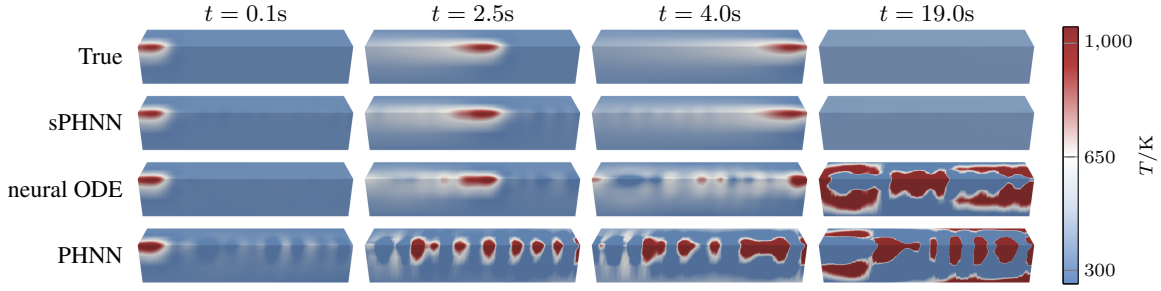


Figure 8. Temperature field predictions on the cuboid domain for a test case with $v = 12.5 \text{ mm s}^{-1}$, $Q = 400 \text{ W}$. The instances selected for this evaluation resulted in the median test error for the corresponding model type. Colors are clipped to remain in the legend’s range.

the sPHNNs consistently converge to temperatures close to thermal equilibrium, the neural ODEs and PHNNs predictions tend to become unstable when one or more augmented dimensions are used. These observations might be explained by the already limited training data becoming even sparser as more dimensions are added to the system. While the data provides enough information about a two-dimensional state space for the models to generalize and allow stable interpolation, the regions of the phase space not covered by the training data grow as more augmented dimensions are added. For the unconstrained models, these regions may contain arbitrary dynamics, including instabilities. In contrast, the stability constraint of the sPHNN enables the safe exploitation of the additional flexibility provided by a higher dimensional state space without running into the same pitfalls of the unconstrained models.

4.5. Additive manufacturing surrogate

Finally, we evaluate the applicability of sPHNNs to higher-dimensional state spaces and build a reduced order model (ROM) as a surrogate of a 3D partial differential equation problem. To this end, we generate field data by numerically solving the heat conduction equation for a moving heat source on a cuboid domain with convective and radiative thermal boundary conditions. The finite element (FE) simulation is designed to model the evolution of the temperature field of a metal additive manufacturing process, see [22]. In total, 25 trajectories are obtained by varying the heat source speed v from 10 mm s^{-1} to 20 mm s^{-1} and power Q from 300 W to 500 W . All trajectories span 20 s, with a non-zero heat source lasting for the initial 2.5 s to 6 s, depending on v . However, directly using the discretized field data would lead to very high-dimensional models and render the training and inference inefficient. Fortunately, the dynamics of complex systems often evolve on lower-dimensional manifolds. We exploit this and use the singular value decomposition (SVD) to find a low-rank approximation of the data. Both temperature and heat source fields are mapped onto 40-dimensional latent spaces, respectively (for details, see App. E). The models are trained on the latent representations of the two trajectories with

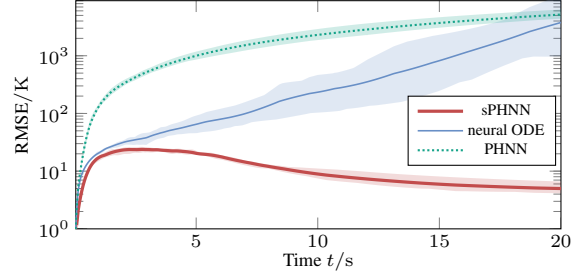


Figure 9. Interquartile mean and range of the RMSEs evaluated with all 25 trajectories of the thermal field data.

$(v, Q) = (10 \text{ mm s}^{-1}, 300 \text{ W})$ and $(20 \text{ mm s}^{-1}, 500 \text{ W})$ using derivative fitting and subsequent fine-tuning with trajectory fitting.

Figure 9 shows the RMSE of the models calculated over all 25 trajectories and the spatial domain. While the sPHNN’s RMSE peaks below 30 K and decreases as the system approaches thermal equilibrium, the errors for neural ODE and PHNN increase rapidly, driven by instabilities in the learned dynamics. This is visible in Fig. 8, which shows the predictions for a test case mapped back to the physical domain. A likely cause of these instabilities is the sparsity of the training data, which leaves gaps in the phase space, allowing unstable dynamics to emerge. The stability constraint in sPHNNs mitigates these issues, ensuring robust performance even with scarce training data.

5. Conclusion

The present work proposes stable port-Hamiltonian NNs for accurate, robust, and reliable identification of nonlinear dynamic systems. They leverage the port-Hamiltonian framework, which provides a basis for model interpretation and the adherence to an energy conservation or dissipation balance with respect to a learned Hamiltonian energy function. Additionally, the approach guarantees the global asymptotic stability of the identified dynamics by constraining the Hamiltonian to be a convex, positive definite Lyapunov function. We demonstrate the viability of the approach using data from synthetic examples, real-world measurements, and complex multiphysics simulation models. While sPHNNs are limited to dynamic systems with a single equilibrium, when

applicable, the stability constraint promotes robust and physically sensible predictions, even with limited training data. We observe superior extrapolation with physically sensible predictions and the capability to exploit augmented dimensions where unconstrained alternative models struggle with instabilities.

Acknowledgements

The work is supported by the joint DFG/FWF Collaborative Research Centre CREATOR (DFG: Project-ID 492661287/TRR 361; FWF: 10.55776/F90) at TU Darmstadt, TU Graz and JKU Linz, Deutsche Forschungsgemeinschaft (DFG, German Research Foundation, Project-ID 492770117), the Graduate School of Computational Engineering at TU Darmstadt, and Hessian.AI.

References

- [1] A. Abbasi, P. N. Kambali, P. Shahidi, and C. Nataraj. “Physics-informed machine learning for modeling multidimensional dynamics”. In: *Nonlinear Dynamics* (2024). DOI: 10.1007/s11071-024-10163-3.
- [2] B. Amos, L. Xu, and J. Z. Kolter. “Input convex neural networks”. In: *Proceedings of the 34th International Conference on Machine Learning*. Ed. by D. Precup and Y. W. Teh. Vol. 70. Proceedings of Machine Learning Research. PMLR, 2017, pp. 146–155.
- [3] M. Barreau and N. Bastianello. “Learning and verifying maximal Taylor-neural Lyapunov functions”. In: *Pre-print under review* (2024). arXiv: 2408.17246.
- [4] C. Beattie, V. Mehrmann, H. Xu, and H. Zwart. “Linear port-Hamiltonian descriptor systems”. In: *Mathematics of Control, Signals, and Systems* 30.4 (2018), p. 17. DOI: 10.1007/s00498-018-0223-3.
- [5] L. Böttcher. “Gradient-free training of neural ODEs for system identification and control using ensemble Kalman inversion”. In: *ICML Workshop on New Frontiers in Learning, Control, and Dynamical Systems*. 2023.
- [6] S. P. Boyd and L. Vandenberghe. *Convex Optimization*. Version 29. Cambridge New York Melbourne New Delhi Singapore: Cambridge University Press, 2023.
- [7] R. T. Q. Chen, Y. Rubanova, J. Bettencourt, and D. K. Duvenaud. “Neural ordinary differential equations”. In: *Advances in Neural Information Processing Systems*. Ed. by S. Bengio, H. Wallach, H. Larochelle, K. Grauman, N. Cesa-Bianchi, and R. Garnett. Vol. 31. Curran Associates, Inc., 2018.
- [8] Y. Chen, Y. Shi, and B. Zhang. “Optimal control via neural networks: A convex approach”. In: *International Conference on Learning Representations*. 2019.
- [9] A. Choudhary, J. F. Lindner, E. G. Holliday, S. T. Miller, S. Sinha, and W. L. Ditto. “Forecasting Hamiltonian dynamics without canonical coordinates”. In: *Nonlinear Dynamics* 103.2 (2021), pp. 1553–1562. DOI: 10.1007/s11071-020-06185-2.
- [10] M. Cranmer, S. Greydanus, S. Hoyer, P. Battaglia, D. Spergel, and S. Ho. “Lagrangian neural networks”. In: *ICLR 2020 Workshop on Integration of Deep Neural Models and Differential Equations*. 2019.
- [11] S. Desai, M. Mattheakis, D. Sondak, P. Protopapas, and S. Roberts. “Port-Hamiltonian neural networks for learning explicit time-dependent dynamical systems”. In: *Physical Review E* 104.3 (2021). DOI: 10.1103/PhysRevE.104.034312. arXiv: 2107.08024.
- [12] E. Dupont, A. Doucet, and Y. W. Teh. “Augmented neural ODEs”. In: *Advances in Neural Information Processing Systems*. Ed. by H. Wallach, H. Larochelle, A. Beygelzimer, F. dAlché-Buc, E. Fox, and R. Garnett. Vol. 32. Curran Associates, Inc., 2019.
- [13] S. Eidnes, A. J. Stasik, C. Sterud, E. Bøhn, and S. Riemer-Sørensen. “Pseudo-Hamiltonian neural networks with state-dependent external forces”. In: *Physica D: Nonlinear Phenomena* 446 (2023), p. 133673. DOI: 10.1016/j.physd.2023.133673.
- [14] N. B. Erichson, M. Muehlebach, and M. W. Mahoney. “Physics-informed autoencoders for Lyapunov-stable fluid flow prediction”. In: *Machine Learning and the Physical Sciences (NeurIPS 2019)*. Vancouver, Canada, 2019.
- [15] S. Greydanus, M. Dzamba, and J. Yosinski. “Hamiltonian neural networks”. In: *Advances in Neural Information Processing Systems*. Ed. by H. Wallach, H. Larochelle, A. Beygelzimer, F. d’Alché-Buc, E. Fox, and R. Garnett. Vol. 32. Curran Associates, Inc., 2019.
- [16] E. Hairer, S. P. Nørsett, and G. Wanner. *Solving Ordinary Differential Equations I: Nonstiff Problems*. 2nd rev. ed. Springer Series in Computational Mathematics 8. Heidelberg ; London: Springer, 2009.

- [17] Q. Hernández, A. Badias, D. Gonzalez, F. Chinesta, and E. Cueto. “Structure-preserving neural networks”. In: *Journal of Computational Physics* 426 (2021), p. 109950. DOI: 10.1016/j.jcp.2020.109950. arXiv: 2004.04653.
- [18] R. A. Horn and C. R. Johnson. *Matrix Analysis*. Second edition, corrected reprint. New York, NY: Cambridge University Press, 2017.
- [19] P. Jin, Z. Zhang, I. G. Kevrekidis, and G. E. Karniadakis. “Learning Poisson systems and trajectories of autonomous systems via Poisson neural networks”. In: *IEEE Transactions on Neural Networks and Learning Systems* 34.11 (2023), pp. 8271–8283. DOI: 10.1109/TNNLS.2022.3148734.
- [20] P. Jin, Z. Zhang, A. Zhu, Y. Tang, and G. E. Karniadakis. “SympNets: Intrinsic structure-preserving symplectic networks for identifying Hamiltonian systems”. In: *Neural Networks* 132 (2020), pp. 166–179. DOI: 10.1016/j.neunet.2020.08.017.
- [21] M. Kannapinn, M. K. Pham, and M. Schäfer. “Physics-based digital twins for autonomous thermal food processing: Efficient, non-intrusive reduced-order modeling”. In: *Innovative Food Science & Emerging Technologies* 81 (2022), p. 103143. DOI: 10.1016/j.ifset.2022.103143.
- [22] M. Kannapinn, F. Roth, and O. Weeger. “Digital twin inference from multi-physical simulation data of DED additive manufacturing processes with neural ODEs”. In: *Pre-print under review* (2024). arXiv: 2412.03295.
- [23] M. Kannapinn, M. Schäfer, and O. Weeger. “TwinLab: A framework for data-efficient training of non-intrusive reduced-order models for digital twins”. In: *Engineering Computations* (2024). DOI: 10.1108/EC23-0855.
- [24] H. K. Khalil. *Nonlinear Systems*. 3rd ed. Upper Saddle River, N.J: Prentice Hall, 2002.
- [25] D. Kingma and J. Ba. “Adam: A method for stochastic optimization”. In: *International Conference on Learning Representations*. 2015.
- [26] R. Kojima and Y. Okamoto. “Learning deep input-output stable dynamics”. In: *Advances in Neural Information Processing Systems*. Ed. by S. Koyejo, S. Mohamed, A. Agarwal, D. Belgrave, K. Cho, and A. Oh. Vol. 35. Curran Associates, Inc., 2022, pp. 8187–8198.
- [27] J. Z. Kolter and G. Manek. “Learning stable deep dynamics models”. In: *Advances in Neural Information Processing Systems*. Ed. by H. Wallach, H. Larochelle, A. Beygelzimer, F. dAlché-Buc, E. Fox, and R. Garnett. Vol. 32. Curran Associates, Inc., 2019.
- [28] Z. Lai, C. Mylonas, S. Nagarajaiah, and E. Chatzi. “Structural identification with physics-informed neural ordinary differential equations”. In: *Journal of Sound and Vibration* 508 (2021), p. 116196. DOI: 10.1016/j.jsv.2021.116196.
- [29] N. Lawrence, P. Loewen, M. Forbes, J. Backstrom, and B. Gopaluni. “Almost surely stable deep dynamics”. In: *Advances in Neural Information Processing Systems* 33 (2020), pp. 18942–18953.
- [30] G. C. Layek. *An Introduction to Dynamical Systems and Chaos*. 1st ed. 2015. New Delhi: Springer India: Imprint: Springer, 2015. DOI: 10.1007/978-81-322-2556-0.
- [31] K. Lee and E. J. Parish. “Parameterized neural ordinary differential equations: Applications to computational physics problems”. In: *Proceedings of the Royal Society A: Mathematical, Physical and Engineering Sciences* 477.2253 (2021), p. 20210162. DOI: 10.1098/rspa.2021.0162.
- [32] C. Legaard, T. Schranz, G. Schweiger, J. Drgoňa, B. Falay, C. Gomes, A. Iosifidis, M. Abkar, and P. Larsen. “Constructing neural network based models for simulating dynamical systems”. In: *Acm Computing Surveys* 55.11 (2023). DOI: 10.1145/3567591.
- [33] D. Liu and Y. Wang. “Multi-fidelity physics-constrained neural network and its application in materials modeling”. In: *Journal of Mechanical Design* 141.12 (2019), p. 121403. DOI: 10.1115/1.4044400.
- [34] M. Lutter, C. Ritter, and J. Peters. “Deep Lagrangian networks: Using physics as model prior for deep learning”. In: *International Conference on Learning Representations*. 2019.
- [35] J. G. Malkin. *Theorie der Stabilität einer Bewegung*. München: R. Oldenbourg, 1959.
- [36] S. Massaroli, M. Poli, M. Bin, J. Park, A. Yamashita, and H. Asama. “Stable neural flows”. In: *Pre-print under review* (2020). arXiv: 2003.08063.
- [37] C. Neary and U. Topcu. “Compositional learning of dynamical system models using port-Hamiltonian neural networks”. In: *Proceedings of the 5th Annual Learning for Dynamics and Control Conference*. Ed. by N. Matni, M. Morari, and G. J. Pappas. Vol. 211. Proceedings of Machine Learning Research. PMLR, 2023, pp. 679–691.
- [38] Y. Okamoto and R. Kojima. “Learning deep dissipative dynamics”. In: *Pre-print under review* (2024). arXiv: 2408.11479.

- [39] J. S. R. Park, S. W. Cheung, Y. Choi, and Y. Shin. “tLaSDI: Thermodynamics-informed latent space dynamics identification”. In: *Computer Methods in Applied Mechanics and Engineering* 429 (2024), p. 117144. DOI: 10.1016/j.cma.2024.117144.
- [40] R. Pascanu, T. Mikolov, and Y. Bengio. “On the difficulty of training recurrent neural networks”. In: *Proceedings of the 30th International Conference on Machine Learning*. Ed. by S. Dasgupta and D. McAllester. Vol. 28. Proceedings of Machine Learning Research. Atlanta, Georgia, USA: PMLR, 2013, pp. 1310–1318.
- [41] S. Ramasinghe, H. Saratchandran, V. Shevchenko, and S. Lucey. “On the effectiveness of neural priors in modeling dynamical systems”. In: *ICML Workshop on New Frontiers in Learning, Control, and Dynamical Systems*. 2023.
- [42] S. M. Richards, F. Berkenkamp, and A. Krause. “The Lyapunov neural network: Adaptive stability certification for safe learning of dynamical systems”. In: *Proceedings of the 2nd Conference on Robot Learning*. Ed. by A. Billard, A. Dragan, J. Peters, and J. Morimoto. Vol. 87. Proceedings of Machine Learning Research. PMLR, 2018, pp. 466–476.
- [43] M. Schoukens, P. Mattson, T. Wigren, and J.-P. Noël. *Cascaded tanks benchmark combining soft and hard nonlinearities*. 2020. DOI: 10.4121/12960104.V1.
- [44] S. Schoukens, P. Mattsson, T. Wigren, and J.-P. Noel. “Cascaded tanks benchmark combining soft and hard nonlinearities”. In: *Workshop on Nonlinear System Identification Benchmarks 2016*. Brussels, Belgium, 2016.
- [45] R. Seydel. *Practical Bifurcation and Stability Analysis*. 3rd ed. Interdisciplinary Applied Mathematics 5. New York: Springer, 2010.
- [46] N. Takeishi and Y. Kawahara. “Learning dynamics models with stable invariant sets”. In: *Proceedings of the AAAI Conference on Artificial Intelligence* 35.11 (2021), pp. 9782–9790. DOI: 10.1609/aaai.v35i11.17176.
- [47] C. Tsitouras. “Runge–Kutta pairs of order 5(4) satisfying only the first column simplifying assumption”. In: *Computers & Mathematics with Applications* 62.2 (2011), pp. 770–775. DOI: 10.1016/j.camwa.2011.06.002.
- [48] A. J. van der Schaft and D. Jeltsema. *Port-Hamiltonian Systems Theory: An Introductory Overview*. Foundations and Trends in Systems and Control 1, 2/3 (2014). Boston Delft: Now, 2014.
- [49] F. Verhulst. *Nonlinear Differential Equations and Dynamical Systems*. Universitext. Berlin New York Paris [etc.]: Springer, 1990.
- [50] R. Wang and R. Yu. “Physics-guided deep learning for dynamical systems: A survey”. In: *Pre-print under review* (2021). arXiv: 2107.01272.
- [51] J. Willard, X. Jia, S. Xu, M. Steinbach, and V. Kumar. “Integrating scientific knowledge with machine learning for engineering and environmental systems”. In: *Acm Computing Surveys* 55.4 (2022). DOI: 10.1145/3514228.
- [52] Z. Zhang, Y. Shin, and G. Em Karniadakis. “GFINNs: GENERIC formalism informed neural networks for deterministic and stochastic dynamical systems”. In: *Philosophical Transactions of the Royal Society A: Mathematical, Physical and Engineering Sciences* 380.2229 (2022), p. 20210207. DOI: 10.1098/rsta.2021.0207.
- [53] Y. D. Zhong, B. Dey, and A. Chakraborty. “Dissipative SymODEN: Encoding Hamiltonian dynamics with dissipation and control into deep learning”. In: *ICLR Workshop on Integration of Deep Neural Models and Differential Equations*. 2020. arXiv: 2002.08860.

A. Proof of stability

This section provides a proof of Theorem 3.1, which describes the essential requirements for achieving stable dynamics with port-Hamiltonian systems. Due to the relevance of convexity to the following discussion, the following Lemma first provides some widely known equivalent formulations of convexity for scalar-valued multivariate functions.

Lemma A.1. *Consider a twice continuously differentiable function $f : \mathbb{R}^n \rightarrow \mathbb{R}$, $\mathbf{x} \mapsto f(\mathbf{x})$. The following statements are equivalent:*

1. f is convex in \mathbf{x} ,
2. $tf(\mathbf{x}_1) + (1-t)f(\mathbf{x}_2) \geq f(t\mathbf{x}_1 + (1-t)\mathbf{x}_2)$, $\forall \mathbf{x}_1, \mathbf{x}_2 \in \mathbb{R}^n$, $\forall t \in [0, 1]$,
3. $\frac{\partial f}{\partial \mathbf{x}} \Big|_{\mathbf{x}_1}^\top (\mathbf{x}_2 - \mathbf{x}_1) \leq f(\mathbf{x}_2) - f(\mathbf{x}_1)$,

For a proof, the reader is referred to [6]. With the notion of convexity established, attention can now be directed to the proof of Theorem 3.1. For convenience, the statement of the theorem is repeated verbatim below:

Theorem A.2. *Consider the PHS Eq. (3) in the unforced case ($\mathbf{u}(t) = \mathbf{0}$), with $\mathbf{J} = -\mathbf{J}^\top$ and $\mathbf{R} = \mathbf{R}^\top$, $\mathbf{R} \succeq 0$:*

$$\dot{\mathbf{x}} = [\mathbf{J}(\mathbf{x}) - \mathbf{R}(\mathbf{x})] \frac{\partial \mathcal{H}}{\partial \mathbf{x}}(\mathbf{x}). \quad (\text{A.1})$$

Suppose the Hamiltonian $\mathcal{H}(\mathbf{x})$ is convex, twice continuously differentiable, and fulfills the following properties:

$$\mathcal{H}(\mathbf{0}) = 0, \quad \frac{\partial \mathcal{H}}{\partial \mathbf{x}} \Big|_{\mathbf{x}=\mathbf{0}} = \mathbf{0}, \quad \frac{\partial^2 \mathcal{H}}{\partial \mathbf{x} \partial \mathbf{x}} \Big|_{\mathbf{x}=\mathbf{0}} \succ 0. \quad (\text{A.2})$$

Then, the system in Eq. (A.1) has a stable equilibrium at $\mathbf{x}(t) = \mathbf{0}$, and all solutions are bounded. Furthermore, the equilibrium is globally asymptotically stable if $\mathbf{R}(\mathbf{x}) \succ 0$.

Proof. Since the gradient of the Hamiltonian vanishes and its Hessian is positive definite, it has a strict local minimum at the origin. This implies the existence of an $R > 0$ such that

$$\mathcal{H}(\mathbf{x}) > \mathcal{H}(\mathbf{0}) = 0 \quad \forall \mathbf{x} \in \{\|\mathbf{x}\| \leq R, \mathbf{x} \neq \mathbf{0}\}. \quad (\text{A.3})$$

Consider the function $g(\mathbf{x}) = \frac{a}{r} \|\mathbf{x}\|$ for some $r \in (0, R]$ with $a = \inf_{\|\mathbf{x}\|=r} \mathcal{H}(\mathbf{x}) > 0$. We claim that g is a lower bound for \mathcal{H} , i.e. $g(\mathbf{x}) \leq \mathcal{H}(\mathbf{x})$ for all $\|\mathbf{x}\| > r$.

Suppose there existed an $\mathbf{x}^* \in \mathbb{R}^n$ that violated the claim, that is $\|\mathbf{x}^*\| > r$ and $g(\mathbf{x}^*) > \mathcal{H}(\mathbf{x}^*)$. Due to the convexity of \mathcal{H} , it holds

$$t\mathcal{H}(\mathbf{x}^*) + (1-t)\mathcal{H}(\mathbf{0}) \geq \mathcal{H}(t\mathbf{x}^* + (1-t)\cdot\mathbf{0}) \quad \forall t \in [0, 1] \quad (\text{A.4})$$

and thus $tg(\mathbf{x}^*) > t\mathcal{H}(\mathbf{x}^*) \geq \mathcal{H}(t\mathbf{x}^*)$. Choosing $t = \frac{r}{\|\mathbf{x}^*\|}$ and applying the definition of g we obtain

$$\frac{r}{\|\mathbf{x}^*\|} g(\mathbf{x}^*) = a > \mathcal{H}\left(\frac{r}{\|\mathbf{x}^*\|} \mathbf{x}^*\right) \geq a. \quad (\text{A.5})$$

This is a contradiction, and therefore g is a lower bound.

With the bound established, showing that \mathcal{H} is radially unbounded is straightforward. For any path $\mathbf{x}(t)$ with $\|\mathbf{x}(t)\| > r$ and $\lim_{t \rightarrow \infty} \|\mathbf{x}(t)\| = \infty$ we have

$$\lim_{t \rightarrow \infty} \mathcal{H}(\mathbf{x}(t)) \geq \lim_{t \rightarrow \infty} g(\mathbf{x}(t)) = \infty. \quad (\text{A.6})$$

To demonstrate the global positive definiteness of \mathcal{H} note that for all $\|\mathbf{x}\| > r$ the lower bound implies $0 < g(\mathbf{x}) \leq \mathcal{H}(\mathbf{x})$. Together with Eq. (A.3), this implies that \mathcal{H} is indeed positive definite for all $\mathbf{x} \in \mathbb{R}^n$.

From the port-Hamiltonian structure of Eq. (A.1) we immediately obtain the decrease condition $\dot{\mathcal{H}} \leq 0$ (see Eq. (5)). Using the \mathcal{H} as a Lyapunov function, we obtain all requirements to conclude *local* stability of the equilibrium. Furthermore, the decrease condition implies that a solution starting at \mathbf{x}_0 cannot leave the sublevel set $\Omega_{\mathcal{H}} = \{\mathbf{x} \in \mathbb{R}^n | \mathcal{H}(\mathbf{x}) \leq \mathcal{H}(\mathbf{x}_0)\}$. Since $\Omega_{\mathcal{H}} \subseteq \Omega_g = \{\mathbf{x} \in \mathbb{R}^n | g(\mathbf{x}) \leq \mathcal{H}(\mathbf{x}_0)\}$ and Ω_g is clearly bounded, all solutions of Eq. (A.1) must be bounded as well.

Finally, to show that *global* asymptotic stability follows from $\mathbf{R} \succ 0$, it remains to be demonstrated that $\dot{\mathcal{H}} < 0$ for all $\mathbf{x} \neq \mathbf{0}$. This is implied by Eq. (5) if $\frac{\partial \mathcal{H}}{\partial \mathbf{x}} \neq \mathbf{0}$ for all $\mathbf{x} \neq \mathbf{0}$. Proving that the gradient of \mathcal{H} vanishes only at the origin is done by contradiction. Assume that there exists an $\mathbf{x}^* \neq \mathbf{0}$ such that $\frac{\partial \mathcal{H}}{\partial \mathbf{x}}|_{\mathbf{x}^*} = \mathbf{0}$. Furthermore, let $\mathbf{x}_0 = \mathbf{0}$. Since \mathcal{H} is convex it follows (see Lemma A.1) that

$$\mathcal{H}(\mathbf{x}_0) - \mathcal{H}(\mathbf{x}^*) \geq \frac{\partial \mathcal{H}}{\partial \mathbf{x}} \Big|_{\mathbf{x}^*}^\top (\mathbf{x}_0 - \mathbf{x}^*) = 0, \quad (\text{A.7})$$

$$\mathcal{H}(\mathbf{x}^*) - \mathcal{H}(\mathbf{x}_0) \geq \frac{\partial \mathcal{H}}{\partial \mathbf{x}} \Big|_{\mathbf{x}_0}^\top (\mathbf{x}^* - \mathbf{x}_0) = 0. \quad (\text{A.8})$$

This implies $\mathcal{H}(\mathbf{x}_0) = \mathcal{H}(\mathbf{x}^*) = 0$. However, since \mathcal{H} is globally positive definite and thus only vanishes at the origin, we have $\mathbf{x}_0 = \mathbf{x}^*$. This is a contradiction as $\mathbf{x}^* \neq \mathbf{0}$, which concludes the proof. \square

B. Experiment hyperparameters

In each experiment presented within this document, the sPHNN, PHNN, and neural ODE models were trained for the same number of steps using identical learning rates. The mean squared error loss function and the ADAM [25] optimizer were used throughout. The model and training hyperparameters, along with the number of model instances trained for statistical evaluation, are provided in Tab. 1. The table also specifies which components of the sPHNN and PHNN were parameterized using NNs (FICNNs and FFNN) and which were chosen to be constant. In each experiment, the PHNNs were defined almost identically to the sPHNNs, with the sole difference being that the normalized FICNN used to represent the Hamiltonian \mathcal{H} was replaced by an unconstrained FFNN. Throughout the first four experiments, all NNs consisted of two hidden layers, each containing 16 neurons. The network width was increased to 32 neurons for the additive manufacturing surrogate.

Table 1. Hyperparameters per experiment. TF and DF refer to trajectory and derivative fitting, respectively. The number of instances trained per model type is listed in the "# inst." column, and n and m denote the number of dimensions of state and input.

Experiment	# training steps	learning rate	# inst.	n	m	parameterization of sPHNNs and PHNNs
Randomly initialized model	-	-	1	2	-	NNs for \mathcal{H} , \mathbf{J} and \mathbf{R}
Spinning rigid body	50 000 DF	1×10^{-3}	10	3	-	NNs for \mathcal{H} and \mathbf{J} ; constant \mathbf{R}
Cascaded tanks	50 000 TF	5×10^{-4}	20	2	1	NN for \mathcal{H} ; $\mathbf{J} = \mathbf{\Omega}$; constant \mathbf{R} and \mathbf{G}
Food processing surrogate	30 000 TF	1×10^{-4}	20	2 to 5	1	NN for \mathcal{H} ; constant \mathbf{J} , \mathbf{R} and \mathbf{G}
Additive manufacturing surrogate	20 000 DF and 10 000 TF	1×10^{-3} 1×10^{-5}	20	40	40	NN for \mathcal{H} ; constant \mathbf{J} , \mathbf{R} and \mathbf{G}

C. Spinning rigid body system

The dynamics of a three-dimensional spinning rigid body example in Sect. 4.2 are described by Euler's rotation equations. Expressing the angular velocity vector $\boldsymbol{\omega} \in \mathbb{R}^3$ in the principle axis coordinate frame, the evolution equation is given by

$$\mathbf{I}\dot{\boldsymbol{\omega}} + \boldsymbol{\omega} \times (\mathbf{I}\boldsymbol{\omega}) = -\mu\boldsymbol{\omega} \quad \forall t > 0. \quad (\text{C.1})$$

Here, $\mathbf{I} = \text{diag}(I_1, I_2, I_3)$ denotes the inertia matrix and μ is a dampening coefficient. By introducing the Hamiltonian

$$\mathcal{H}(\boldsymbol{\omega}) = \frac{1}{2}I_1\omega_1^2 + \frac{1}{2}I_2\omega_2^2 + \frac{1}{2}I_3\omega_3^2, \quad (\text{C.2})$$

which describes its kinetic energy E , the system can be rewritten as a PHS in the form of Eq. (3):

$$\begin{bmatrix} \dot{\omega}_1 \\ \dot{\omega}_2 \\ \dot{\omega}_3 \end{bmatrix} = \left(\underbrace{\begin{bmatrix} 0 & -\frac{I_3}{I_1 I_2} \omega_3 & \frac{I_2}{I_3 I_1} \omega_2 \\ \frac{I_3}{I_1 I_2} \omega_3 & 0 & -\frac{I_1}{I_2 I_3} \omega_1 \\ -\frac{I_2}{I_3 I_1} \omega_2 & \frac{I_1}{I_2 I_3} \omega_1 & 0 \end{bmatrix}}_{\mathbf{J}(\boldsymbol{\omega})} - \underbrace{\mu \begin{bmatrix} \frac{1}{I_1^2} & 0 & 0 \\ 0 & \frac{1}{I_2^2} & 0 \\ 0 & 0 & \frac{1}{I_3^2} \end{bmatrix}}_{\mathbf{R}} \right) \frac{\partial \mathcal{H}}{\partial \boldsymbol{\omega}}. \quad (\text{C.3})$$

Here, the structure matrix \mathbf{J} is a matrix-valued function of the state variable $\boldsymbol{\omega}$.

We generated $(\boldsymbol{\omega}, \dot{\boldsymbol{\omega}})$ pairs for training by evaluating Eq. (C.1) for varying $\boldsymbol{\omega}$. To simulate a measurement process, we selected $\boldsymbol{\omega}$ values from 50 s long numerically integrated trajectories, using 10 randomly chosen initial conditions $\boldsymbol{\omega}(0) \in [0, 1]^3$ with parameters $\mathbf{I} = \text{diag}(1, 2, 3)$ and $\mu = 0.01$. A representative trajectory of $\boldsymbol{\omega}$ is shown in Fig. 10.

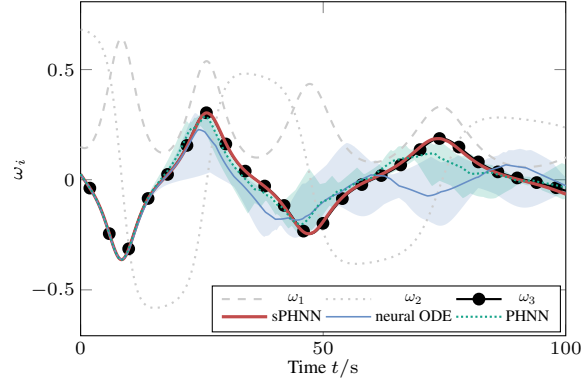


Figure 10. Representative training trajectory for spinning rigid body, including interquartile mean and range of model predictions for ω_3 .

D. Thermal food processing surrogate data

This section provides additional details about the data used in Sect. 4.4, which is a subset of the data generated and used by Kannapinn et al. [21] in the creation of ROMs. The dataset describes the thermal processing of chicken breasts in a convection oven and was generated via the simulation of a soft-matter model for meats implemented in COMSOL Multiphysics. Each trajectory in the data set describes the temperature history at two points inside the full order model. These result from a predefined excitation signal that controls the oven temperature. The probe points are situated in the center and close to the surface of the food item, with the corresponding temperatures labeled as T_A and T_B , respectively. To facilitate cross-referencing, the alphanumeric identifiers used by Kannapinn et al. [21] for the individual trajectories are retained. The training data consists of trajectories 745 and 795. They use an amplitude-modulated pseudo-random binary sequence (APRBS) and a multi-sine as the excitation signal T_{oven} . Figure 11 (left and middle) illustrates T_{oven} along with the core and surface temperatures for both trajectories. In our experiment, the test group AP15 [21] is utilized as test data. It comprises 15 trajectories with APRBS excitations, specifically selected to ensure an even distribution of amplitudes and median values. This selection provides a fair evaluation of the models across the relevant temperature spectrum. Figure 11 (right) shows an exemplary test trajectory, including the predictions for T_A from all models using 3 augmented dimensions. All trajectories span 1395 s and consist of 280 samples. The data is normalized for training to ensure the numerical values are of magnitude one. For this, an affine transformation is applied to T_{oven} , T_A , and T_B individually. It shifts the ambient temperature to a value of zero and rescales the signal to have unit variance. The scaling and shifting factors are calculated using only the training data to ensure that the test data does not influence the training procedure.

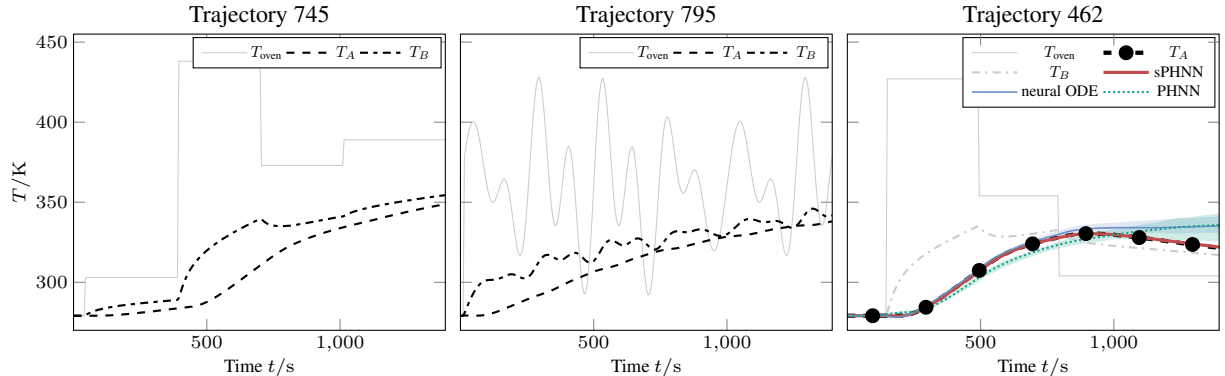


Figure 11. Left and middle: Training trajectories. Right: Exemplary test trajectory with interquartile mean and range of the model predictions for T_A .

E. Thermal field data

The following describes the method for dimensionality reduction of the field data applied in Sect. 4.5. The process is first described for general field data given as a matrix $\mathbf{A} = [\mathbf{a}_0, \dots, \mathbf{a}_N]^\top$ of N snapshots $\mathbf{a}_i \in \mathbb{R}^M$, where N is the number of snapshots and M is the number of FE nodes. To identify the dominant modes of the data, we perform a SVD of \mathbf{A} :

$$\mathbf{A} = \mathbf{U}\mathbf{\Sigma}\mathbf{V}^\top \in \mathbb{R}^{N \times M}, \quad (\text{E.1})$$

where $\mathbf{U} \in \mathbb{R}^{N \times N}$ and $\mathbf{V} \in \mathbb{R}^{M \times M}$ are unitary matrices and $\mathbf{\Sigma} \in \mathbb{R}^{N \times M}$ is a rectangular diagonal matrix containing the singular values $\sigma_1 \geq \dots \geq \sigma_N$ on its diagonal. Dimensionality reduction is achieved by truncating the SVD $\mathbf{A} \approx \tilde{\mathbf{U}}\tilde{\mathbf{\Sigma}}\tilde{\mathbf{V}}^\top$, where $\tilde{\mathbf{U}} \in \mathbb{R}^{N \times k}$ and $\tilde{\mathbf{V}} \in \mathbb{R}^{M \times k}$ contain the first k columns of \mathbf{U} and \mathbf{V} , and $\tilde{\mathbf{\Sigma}} = \text{diag}(\sigma_1, \dots, \sigma_k)$ is the truncated matrix of the dominant singular values. The dominant modes in the data are then given by $\mathbf{M} = c\tilde{\mathbf{V}}$. Here, the scaling factor c is the standard deviation of the elements in $\tilde{\mathbf{U}}\tilde{\mathbf{\Sigma}}$. This scaling ensures that the latent trajectories will have unit variance. To map a latent state $\mathbf{x} \in \mathbb{R}^k$ to the full order field $\mathbf{X} \in \mathbb{R}^M$ we compute:

$$\mathbf{X} = \mathbf{M}\mathbf{x}. \quad (\text{E.2})$$

Conversely, to map from the full-order field to the latent space, we solve the least-squares regression problem:

$$\mathbf{x} = \arg \min_{\mathbf{x}} \|\mathbf{X} - \mathbf{M}\mathbf{x}\|. \quad (\text{E.3})$$

In Sect. 4.5, we consider two fields: The thermal field describing the state of the system and the excitation given by the heat source field. For each, a separate SVD is performed to compute \mathbf{M}_T and \mathbf{M}_Q using the respective snapshots from the two training trajectories.

To fully leverage the benefits of sPHNNs, it is essential to ensure that the absence of a heat source is encoded as the zero-vector in the corresponding latent space. Since the mapping from the latent space Eq. (E.2) is linear, and $\mathbf{X}_Q = \mathbf{0}$ corresponds to the absence of a heat source in the full order space, this requirement is automatically fulfilled. However, for applications where a nonzero state \mathbf{X}^* describes the absence of an external energy source or general nonlinear latent mappings (such as autoencoders), the condition can be met by applying a constant translation in the latent space, which shifts the encoded state \mathbf{x}^* to the origin. In Sect. 4.5, we use this method to ensure that the thermal equilibrium corresponds to the origin of the temperature latent space. While this is not strictly necessary, knowledge of the equilibrium location in the latent space enables its integration into the sPHNN’s architecture by fixing the stable equilibrium position.

Finally, we note that alternative dimensionality reduction techniques could be applied in Sect. 4.5. In preliminary experiments, we explored the use of autoencoders for this purpose. Although autoencoders offer advantages over the linear SVD regarding achievable compression rates, they exhibited poor extrapolation performance when trained on sparse data. This issue could potentially be mitigated by training the autoencoders with additional synthetic data, which would not necessitate costly simulations; however, further research is needed to explore this approach.